A Modified Interactive Spectral Smooth Temperature Emissivity Separation Algorithm for Low-Temperature Surface

Yongming Du, Hua Li, Biao Cao, Zunjian Bian, Jianming Zhao, Qing Xiao, Qinhuo Liu, Yijian Zeng, and Zhongbo Su

***Abstract*— When ground-leaving radiance from low-temperature surface is similar to downwelling radiance from the sky, the singular values arise in the retrieved land surface emissivity (LSE) at some specific spectral bands. In addition, too many singular values eventually cause temperature/emissivity separation algorithms to fail. To reduce the occurrence of these singular points, we formulate two indices, including the land-atmosphere radiance contrast index (LACI) and neighbor band contrast index (NBCI). LACI characterizes the contrast between surface radiance and sky downwelling radiance. NBCI characterizes the contrast between the radiance at neighboring bands. These two indices are used as filters to select bands which participate in the iterative spectrally smooth calculation. Thus, we modify the iterative spectrally smooth temperature and emissivity separation (ISSTES) algorithm for low-temperature surfaces. Two methods have been used to evaluate the modified algorithm. First, numerical experiments are conducted to evaluate if the modified algorithm can accurately retrieve the "true" LSE from the simulated data. Second, an artificial low-temperature surface cooled by liquid nitrogen is measured to validate the modified algorithm. The results show that the modified algorithm can effectively avoid singular values, and behaves much better than the original algorithm with errors of less than 0.01 in retrieved emissivity when applied to low-temperature regions, while the modified algorithm brings limited improvement in retrieved temperature.**

***Index Terms*— Emissivity, hyperspectral thermal infrared (TIR), low temperature, temperature and emissivity separation (TES).**

I. Introduction

LAND surface emissivity (LSE) is a basic parameter in thermal infrared (TIR) remote sensing. The concept of LSE has been well discussed [1]–[4]. LSE is the key parameter in radiation budget estimation, energy balance research and water circle studies for land-atmosphere systems [5]–[7]. As an intrinsic property of natural materials, LSE was used for mineral mapping and geological studies [8]–[10], [42]. A recent study showed that LSE can be used to classify plant species [38]–[40].

Emissivity retrieval from radiometric measurements is an ill-posed problem that obtains N spectral radiance measurements and needs to find $N+1$ unknowns (i.e., N emissivities and one temperature) [16]. In recent decades, considerable efforts have been devoted to solving temperature and emissivity separation (TES). Many algorithms have been developed, including the temperature-independent spectral indices method [20], spectral ratio method [21], two-temperature method [22], reference channel method [23], TES method for Advanced Spaceborne Thermal Emission and Reflection Radiometer (ASTER) [25], gray-body method [26], alpha emissivity method [27], day/night method [28], stepwise refining method [29], piecewise linear regression [30], neural network method [31], [32], and spectral smooth method [16], [17], [33]. For comprehensive reviews, please refer to [18] and [19].

The iterative spectrally smooth temperature and emissivity separation (ISSTES) algorithm was proposed by Borel [16], [17]. It is widely used to retrieve land surface temperature (LST) and emissivity from ground-based and airborne/spaceborne hyperspectral TIR data. For normal temperature surfaces, ISSTES has an excellent accuracy with an error of 0.0004 in retrieved emissivity[34]. ISSTES has been accepted as a standard to examine the accuracy of new algorithms (NAs) [29]–[33].

Low-temperature regions on the Earth, such as polar ice caps and frozen soils on the Tibet Plateau, often respond to global change more significantly than other regions. These low-temperature regions play an indicative role in global change research [11]–[15]. For low-temperature regions, when the downward radiance is comparable to the surface radiance, the retrieved emissivity error increases, and a singular value occurs at some specific bands. Until now, there have been few studies on the emissivity retrievals of low-temperature targets.

Fortunately, due to the narrow spectrum of downward atmospheric radiation, some bands of atmospheric radiation are close to the surface radiation in hyperspectral infrared measurements; meanwhile, others are still in the normal range which differs from the surface radiation far enough to retrieve

Manuscript received October 9, 2019; revised December 30, 2019 and March 13, 2020; accepted March 13, 2020. This work was supported in part by Chinese Natural Science Foundation under Project 41571359, Project 41671366, Project 41501366, and Project 41571357, and in part by the National Key Research and Development Program under Grant 2018YFA0605503. *(Corresponding author: Hua Li.)*

Yongming Du, Hua Li, Biao Cao, Zunjian Bian, Qing Xiao, and Qinhuo Liu are with the State Key Laboratory of Remote Sensing Science, Aerospace Information Research Institute (AIR), Chinese Academy of Sciences (CAS), Beijing 100101, China, and also with the Joint Center for Global Change Studies (JCGCS), Beijing 100875, China (e-mail: lihua@aircas.ac.cn).

Jianming Zhao is with the Beijing Institute of Remote Sensing Information, Beijing 100192, China.

Yijian Zeng and Zhongbo Su are with the Faculty of Geo-Information Science and Earth Observation, University of Twente, 7514 Enschede, The Netherlands.

Color versions of one or more of the figures in this article are available online at http://ieeexplore.ieee.org.

Digital Object Identifier 10.1109/TGRS.2020.2982960

emissivity precisely. Finding these normal bands is the critical step for improving the TES algorithm for low-temperature regions. In this article, we define two indices. One characterizes the contrast between the downward radiance and surface radiation, and the other characterizes the contrast between the downward radiance at two neighboring bands. These two indices are used to select suitable bands to participate in the ISSTES operation and avoid singular values. The modified ISSTES algorithm is evaluated synthetically with numerical experimental data generated by MODTRAN 4.0 with thermodynamic initial guess retrieval (TIGR) atmospheric profile data and the John Hopkins University (JHU) spectra library database. A field measurement was conducted to verify the NA. This article is organized as follows. Section II reviews the theoretical background and algorithm structure of the ISSTES algorithm. Section III introduces the modification of the algorithm. Section IV discusses the performance of the algorithm. Section V describes the field measurement to verify the NA, and Section VI provides the summary of the full article.

II. Theoretical Background

A. Theory Basis

The spectral radiance received by the spectrometer can be seen as the sum of three components, which are the radiance emitted at the surface, the reflectance of the atmospheric downward radiance at the surface, and the atmospheric upward radiance. The radiative transfer equation (RTE) in the TIR band can be written as follows:

$$\begin{aligned} L_\lambda(\theta_r, \Phi_r) = {} & \tau_\lambda(\theta_r, \Phi_r)\varepsilon_\lambda(\theta_r, \Phi_r)B_\lambda(\mathrm{T}_s) \\ & + \tau_\lambda(\theta_r, \Phi_r)\int_{2\pi}(\rho_\lambda(\theta_i, \Phi_i, \theta_r, \Phi_r)) \\ & \times L_{\mathrm{atm}\downarrow,\lambda}(\theta_i, \Phi_i)\cos\theta_i d\Omega \\ & + L_{\mathrm{atm}\uparrow,\lambda}(\theta_r, \Phi_r) \end{aligned} \quad (1)$$

where $L_\lambda(\theta_r, \Phi_r)$ is the spectral radiance received by the spectrometer at band λ at zenith angle θ_r and at azimuth angle Φ_r; $\tau_\lambda(\theta_r, \Phi_r)$ is the spectral transmittance of the atmosphere from the surface to the spectrometer; $\varepsilon_\lambda(\theta_r, \Phi_r)$ is the spectral directional emissivity; $B_\lambda(\mathrm{T}_s)$ is the spectral radiance emitted by a blackbody at surface temperature T_s and can be calculated with Planck's law; $\rho_\lambda(\theta_i, \Phi_i, \theta_r, \Phi_r)$ is the surface's bidirectional reflection distribution function (BRDF); $L_{\mathrm{atm}\downarrow,\lambda}(\theta_i, \Phi_i)$ is the downward spectral radiance emitted by the total atmosphere at the illumination zenith angle θ_i and azimuth angle Φ_i; and $L_{\mathrm{atm}\uparrow,\lambda}(\theta_r, \Phi_r)$ is the upward spectral radiance emitted by the atmosphere from the surface to the spectrometer.

Equation (1) can be reformed to the following equation:

$$\begin{aligned} L_\lambda(\theta_r, \Phi_r) = {} & \tau_\lambda(\theta_r, \Phi_r)L_{\mathrm{leaving},\lambda}(\theta_r, \Phi_r) \\ & + L_{\mathrm{atm}\uparrow,\lambda}(\theta_r, \Phi_r) \end{aligned} \quad (2\text{-a})$$

$$\begin{aligned} L_{\mathrm{leaving},\lambda}(\theta_r, \Phi_r) = {} & \varepsilon_\lambda(\theta_r, \Phi_r)B_\lambda(\mathrm{T}_s) \\ & + \int_{2\pi}(\rho_\lambda(\theta_i, \Phi_i, \theta_r, \Phi_r)) \\ & \times L_{\mathrm{atm}\downarrow,\lambda}(\theta_i, \Phi_i)\cos\theta_i d\Omega \end{aligned} \quad (2\text{-b})$$

where $L_{\mathrm{leaving},\lambda}$ is the ground leaving radiance, which is composed of emission items and reflectance items and can be measured directly at the bottom of the atmosphere (BOA). Once the atmospheric transmittance and upward radiance are determined, the land-leaving radiance spectra can also be determined from the airborne/spaceborne measured radiance spectra. This process is called atmospheric correction

$$\begin{aligned} & L_{\mathrm{leaving},\lambda}(\theta_r, \Phi_r) \\ & \quad = (L_\lambda(\theta_r, \Phi_r) - L_{\mathrm{atm}\uparrow,\lambda}(\theta_r, \Phi_r))/\tau_\lambda(\theta_r, \Phi_r). \end{aligned} \quad (3)$$

To simplify questions, the surface is often assumed to be Lambertian. Then, (2-b) can be simplified as follows:

$$L_{\mathrm{leaving},\lambda} = \varepsilon_\lambda B_\lambda(\mathrm{T}_s) + \rho_\lambda \int_{2\pi} L_{\mathrm{atm}\downarrow,\lambda}(\theta_i, \Phi_i)\cos\theta_i d\Omega \quad (4)$$

where $\int_{2\pi} L_{\mathrm{atm}\downarrow,\lambda}(\theta_i, \Phi_i)\cos\theta_i d\Omega$ is the hemispherical integration of atmospheric downward radiation, denoted as $L_{\mathrm{atm}\downarrow,\lambda}$. According to Kirchhoff's law, $\rho_\lambda = 1 - \varepsilon_\lambda$. Then, (4) can be written as follows:

$$L_{\mathrm{leaving},\lambda} = \varepsilon_\lambda B_\lambda(\mathrm{T}_s) + (1 - \varepsilon_\lambda)L_{\mathrm{atm}\downarrow,\lambda}. \quad (5)$$

Reforming (5), we can obtain the surface temperature formula as follows:

$$\mathrm{T}_s = B_\lambda^{-1}((L_{\mathrm{leaving},\lambda} - (1 - \varepsilon_\lambda)L_{\mathrm{atm}\downarrow,\lambda})/\varepsilon_\lambda) \quad (6)$$

where $B_\lambda^{-1}()$ is the inverse Planck function.

Then, emissivity can be expressed as the following equation:

$$\varepsilon_\lambda = (L_{\mathrm{leaving},\lambda} - L_{\mathrm{atm}\downarrow,\lambda})/(B_\lambda(\mathrm{T}_s) - L_{\mathrm{atm}\downarrow,\lambda}) \quad (7\text{-a})$$

$$\begin{aligned} \varepsilon_\lambda = {} & (L_\lambda(\theta_r, \Phi_r) - \tau_\lambda(\theta_r, \Phi_r)L_{\mathrm{atm}\downarrow,\lambda} \\ & - L_{\mathrm{atm}\uparrow,\lambda}(\theta_r, \Phi_r))/(\tau_\lambda(\theta_r, \Phi_r)(B_\lambda(\mathrm{T}_s) - L_{\mathrm{atm}\downarrow,\lambda})) \end{aligned} \quad (7\text{-b})$$

where $L_{\mathrm{atm}\downarrow,\lambda}$ can be given by the atmospheric correction module. Many studies have discussed atmospheric correction. Ground-based measurements adopt (7-a), while airborne/spaceborne measurements adopt (7-b). The remaining question is how to solve the TES. Unfortunately, this requires solving $N + 1$ unknowns (N emissivity values and one temperature) with N equations (N measured spectral radiance), which is a typical ill-posed question. Some constraints must be posed as prior knowledge to make the equations soluble.

B. Review of ISSTES

The individual molecules in a gas are isolated free and tend to emit a narrow spectral radiance, while solid molecules are fixed in the crystal lattice and tend to emit a wide spectral radiance. There is a sharp contrast of the TIR emissivity spectral feature between a solid and gas. Since the LSE spectrum is rather smooth compared with the spectral features introduced by the atmosphere, when the estimated temperature is not the best, there is a residual of the rugged downward radiance spectral curve in the emissivity. Then, the contrast between neighboring bands' emissivities can be used as constraints to

solve the TES problem, which is the main idea of ISSTES [16]. The smoothness of spectral emissivity is defined as follows:

$$\sigma = \mathrm{STDEV}\left(\varepsilon_\lambda - \frac{\varepsilon_{\lambda-1} + \varepsilon_\lambda + \varepsilon_{\lambda+1}}{3}\right) \tag{8}$$

where σ is the smoothness. ***STDEV*** is the standard deviation (stdev) operator.

The main steps of ISSTES are as follows.

1) Given a typical value of 0.95 for the emissivity, we can obtain the estimated temperature T_{est} by (6) and can generate a series of temperatures in a range around T_{est}, denoted as T_n, $n = 1, 2, \ldots, N$.
2) Calculate a series of spectral emissivities ε_n by (7) according to T_n.
3) Calculate a smoothness series by (8), denoted as σ_n, according to ε_n.
4) Obtain the best-estimated temperature T_{opt} by searching the minimum smoothness.

Once the best-estimated temperature is given, the emissivity spectrum can be calculated by (7).

Borel [17] proposed another version of the TES algorithm in which the difference between the calculated and measured radiance was used as the criterion to determine the best temperature. Theoretically, the advantage of this method is that it can extend the work band to the low atmospheric transmittance region instead of being suitable for the low temperature. Because of the extensive citation and verification of the ISSTES algorithm [29]–[34], [37], we choose the emissivity smoothness as the criterion in our algorithm.

C. Effects of Low Temperature

The ISSTES algorithm performs well for normal-temperature targets [34]. In practical applications, we find that it suffers from many singular values when applied to low-temperature targets. Two main mechanisms can explain the effect of low temperature on the ISSTES.

1) Due to the surface-emission radiance reduction, the contrast between the atmospheric downward radiation and the radiation leaving the low-temperature surface is weak. When the downward radiance from the atmosphere is close to the ground leaving radiance, the denominator terms of (7-a) and (7-b) will be close to 0, resulting in instability of the division. The effects of instrument noise and calibration error will be amplified, which leads to the occurrence of singular values.
2) For the low-temperature regions on the Earth, the atmosphere is often cold and dry. The characteristics of the absorption/emission lines caused by water vapor or other gases are faded. There is a weak contrast between the land and atmosphere emissivity spectral features. This phenomenon will undermine the assumption of the ISSTES algorithm. If the downwelling radiance exceeds ground leaving radiance for some bands and be less than the blackbody's radiance of the surface temperature, the emissivity will be calculated by (7-a) to be a negative value.

III. Modification of the Algorithm

The main idea of our study is to develop indices to describe the two main mechanisms that reduce the accuracy of the ISSTES algorithm caused by the low-temperature effect. We construct a weight function based on the developed indices and give different weight coefficients to different bands for estimating the temperature. We use interpolation technology to fill the singular band emissivity calculation step.

A. Land-Atmosphere Radiance Contrast Index (LACI)

To characterize the contrast levels of ground-atmosphere radiance, we design an index, land-atmosphere radiance contrast index (LACI), which is formulated as (9). It is the ratio of the absolute value of the difference between the ground leaving radiance and the downward radiance from the atmosphere to the ground leaving radiance. This index depends on the wavelength. Normally, LACI_λ varies in the range 0–1. When LACI_λ is 0, the downward radiance from the atmosphere equals the ground leaving radiance at band λ. As LACI_λ increases, the land-atmosphere radiance contrast becomes stronger

$$LACI_\lambda = \boldsymbol{ABS}(L_{\mathrm{leaving},\lambda} - L_{\mathrm{atm}\downarrow,\lambda})/L_{\mathrm{leaving},\lambda} \tag{9}$$

where ***ABS***() is the absolute value operator.

The mean value of this index, $\overline{\mathrm{LACI}}$, can be derived by averaging the LACI_λ

$$\overline{\mathrm{LACI}} = \left(\sum_{\lambda=1}^{N_\mathrm{M}} \mathrm{LACI}_\lambda\right) \Big/ N_\mathrm{M} \tag{10}$$

where N_M is the number of bands within the measurement spectral range.

B. Neighbor Band Contrast Index (NBCI)

We also designed an index, neighbor band contrast index (NBCI), to measure the contrast between the atmospheric downwelling radiance at adjacent bands [see(11)]. When NBCI_λ is 0, the atmospheric downward radiation spectrum curve is flat at band λ, and band λ is not suitable for inverting the emissivity. As NBCI_λ increases, the sharper spectral contrast of atmospheric downward radiation is reflected in the ground leaving radiance, resulting in resolving TES robustly

$$\mathrm{NBCI}_\lambda = \boldsymbol{ABS}(2\times L_{\mathrm{atm}\downarrow,\lambda} - L_{\mathrm{atm}\downarrow,\lambda-1} - L_{\mathrm{atm}\downarrow,\lambda+1})/(2\times L_{\mathrm{leaving},\lambda}). \tag{11-a}$$

NBCI_λ represents the extent to which downwelling atmospheric radiance at the current spectral position deviates from adjacent bands. The mean value of this index, $\overline{\mathrm{NBCI}}$, can be calculated by averaging the NBCI_λ

$$\overline{\mathrm{NBCI}} = \left(\sum_{\lambda=1}^{N_\mathrm{M}} \mathrm{NBCI}_\lambda\right) \Big/ N_\mathrm{M}. \tag{11-b}$$

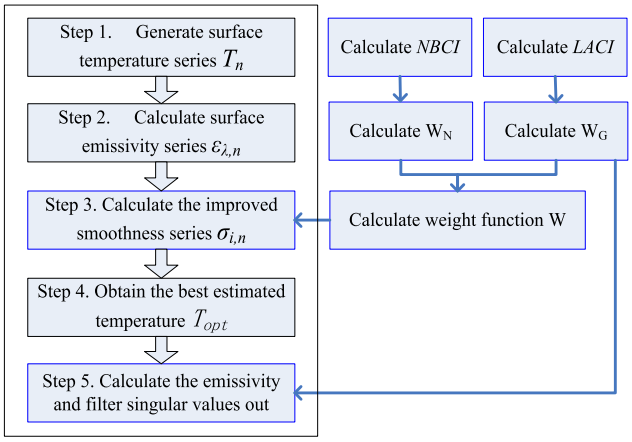

Fig. 1. Modified ISSTES algorithm workflow chart.

C. Weight Function

Even though TIR hyperspectral data provide rich information, not all bands provide useful information for solving TES. Instead, some bands may introduce errors for low-temperature targets. The ISSTES is based on the assumption that the retrieved emissivity is spectral rough until the temperature is right. The spectral roughness of the retrieved emissivity is the residual of downwelling radiance. These bands with low NBCI_λ will produce smooth emissivity regardless what value the temperature is given. So they provide little contribution for TES. These bands with low LACI_λ even bring errors in solving TES due to the instability of division by a too small denominator. We design the weight function [see(12)] to reflect each band's contribution for solving TES. The weight function is composed of two parts. One is the binarization function: when LACI_λ is greater than or equal to a threshold C_a, the binarization function returns 1; otherwise, it returns 0. The other is the normalized NBCI_λ

$$W_\lambda = W_{\mathrm{G},\lambda} \times W_{N,\lambda} \tag{12-a}$$

$$W_{\mathrm{G},\lambda} = \begin{cases} 1, & |\mathrm{LACI}_\lambda \geq C_a \\ 0, & |\mathrm{LACI}_\lambda < C_a \end{cases} \tag{12-b}$$

$$W_{N,\lambda} = \mathrm{NBCI}_\lambda / \mathrm{MAX(NBCI)}. \tag{12-c}$$

Determining the threshold C_a is discussed in Section IV-B.

D. Modified Algorithm Construction

We retain the main structure of the ISSTES algorithm, which was mentioned in Section II-B. We modified the ISSTES process with two steps: step 3 and step 5 (Fig. 1).

In step 3, the weight function [see(12)] is used to calculate the smoothness of the spectral emissivity. Equation (8) is rewritten as (13) in the modified algorithm

$$\sigma = \mathrm{STDEV}\left(\left(\varepsilon_\lambda - \frac{\varepsilon_{\lambda-1} + \varepsilon_\lambda + \varepsilon_{\lambda+1}}{3}\right) \times \mathrm{W}_\lambda\right). \tag{13}$$

When $W_{\mathrm{G},\lambda} = 0$, the emissivity at band λ is singular. In step 5, after obtaining the emissivity spectrum by (7), we filter out the singular values and interpolate the neighboring bands' emissivity for substitution using (14), where we assume that the atmospheric emission band is narrower than the instrument's band

$$\varepsilon_{i,\lambda} = \begin{cases} \varepsilon_\lambda, & |W_{\mathrm{G},\lambda} = 1 \\ (\varepsilon_{\lambda-1} + \varepsilon_{\lambda+1})/2, & |W_{\mathrm{G},\lambda} = 0. \end{cases} \tag{14}$$

IV. Algorithm Performance

We evaluate the NA in two aspects. First, compared with the original ISSTES algorithm, we examine the accuracy of the NA under various conditions, including different LSTs, different ground atmospheric radiation contrast conditions and different neighboring band radiation contrast conditions. Second, we analyze the sensitivity of the NA to instrument noise and atmospheric correction error. We use simulated data to perform the evaluation. The following measures are adopted to describe the accuracy of the algorithm, including the absolute value error of the estimated temperature for an individual retrieval

$$e_{T,\mathrm{in}} = |\mathrm{T_{est}} - \mathrm{T_{true}}|. \tag{15}$$

The root-mean-square error (RMSE) of the retrieved temperature for a retrieval group with N_D members is

$$\mathrm{RMSE_{T,gp}} = \sqrt{\frac{\sum_{i=1}^{N_\mathrm{D}} (\mathrm{T_{est},}_i - \mathrm{T_{true},}_i)^2}{N_\mathrm{D}}}. \tag{16}$$

The RMSE of the retrieved and true emissivity difference for one individual emissivity spectrum with N_M bands is

$$\mathrm{RMSE}_{\varepsilon,\mathrm{in}} = \sqrt{\frac{\sum_{j=1}^{N_\mathrm{M}} (\varepsilon_{\mathrm{est},j} - \varepsilon_{\mathrm{true},j})^2}{N_\mathrm{M}}}. \tag{17}$$

The RMSE of the retrieved and true emissivity difference for a data set with N_D member emissivity spectra with N_M bands is

$$\mathrm{RMSE}_{\varepsilon,\mathrm{gp}} = \sqrt{\frac{\sum_{i=1}^{N_\mathrm{D}} \sum_{j=1}^{N_\mathrm{M}} (\varepsilon_{\mathrm{est},i[j]} - \varepsilon_{\mathrm{true},i[j]})^2}{N_\mathrm{D} \times N_\mathrm{M}}} \tag{18}$$

where $\mathrm{T_{est}}$ and $\mathrm{T_{true}}$ are the estimated and true temperature, respectively, and $\varepsilon_{\mathrm{est}}$ and $\varepsilon_{\mathrm{true}}$ are the estimated and true emissivity, respectively. In the following analysis and evaluation, the input temperature and emissivity values for simulation are taken as the true temperature and emissivity.

A. Simulated Data

Before evaluating the modified algorithm, we simulate land leaving radiance spectra and downwelling radiance spectra using MODTRAN 4.0 with TIGR atmospheric profile V3 data set [35] and the JHU spectra library database [36]. As we are concerned with the low-temperature situation, we set the surface temperature from 240 to 270 K at intervals of 10 K. Galve *et al.* [44] illustrated that there is a statistical correlation between the LST and temperatures of the first layer of atmospheric profile (T0). LST varies in the range of T0±20K. Therefore, we select 1535 representative atmospheric profiles from TIGR data set with the first-layer temperature in the range of [220K, 290K], They are adopted as inputs for the MODTRAN 4.0 code to generate

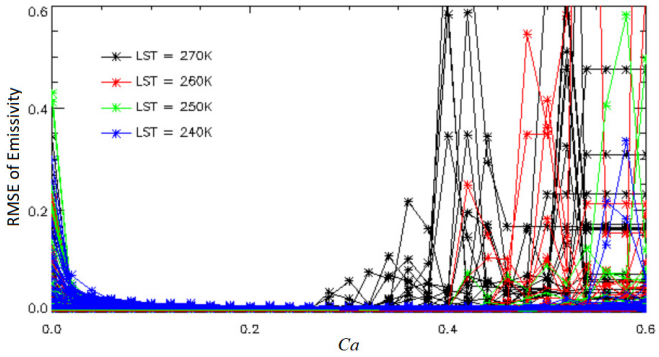

Fig. 2. Emissivity RMSE changed with the threshold C_a.

1535 downwelling radiance spectra. Five typical surface (including soil, snow, man-made object, limestone, and sandstone, noted as SP1–SP5, respectively) emissivity spectra selected from the JHU spectral library are used to mimic the land leaving radiance. In the simulation process, the spectral resolution is set to 1 cm^{-1}, the noise-equivalent temperature is set to 0.3 K, and the spectral range is set to 800–1250 cm^{-1} (8.0–12.5 μm). Then, we acquire 1535 × 5 × 4 pairs of simulation data, including the atmospheric downwelling radiance spectra and ground leaving radiance spectra.

B. Determining the Value of C_a

To determine the optimal value of C_a, we change the C_a value in the range from 0 to 0.6 with an interval of 0.02. Random noise of 0.3 K noise-equivalent temperature difference (NETD) is added to the simulation data. Then, we retrieve the emissivity from the simulation data using the NA with different *Ca*. Then, the relationship between the *Ca* value and emissivity RMSE is obtained (Fig. 2). *Ca* is the threshold of LACI, which was defined as (9). Under normal circumstances, atmospheric downwelling radiance is small relative to the land leaving radiance and LACI tends to be high. For low-temperature surface, because of the weak radiance omitted from surface, when $L_{\text{atm}\downarrow,\lambda}$ is close to $L_{\text{leaving},\lambda}$ in atmospheric emission bands, LACI approaches zero and the retrieved emissivity falls in the singular value. *Ca* is designed to screen these abnormal bands [see (12-b)]. When the *Ca* is too low, the retrieved emissivity will suffer from instability of division due to the low LACI. When the C_a is too high, the low LACI will be abandoned meanwhile some high NBCI will also be abandoned by the weight function. The low NBCI will undermine the precision of retrieved emissivity. When the value of C_a is smaller than 0.05 or larger than 0.3, the emissivity RMSE is relatively large (Fig. 2). Hereafter, we select 0.2 as the C_a value for the analysis.

C. Accuracy Evaluation

After adding random noise with an NETD of 0.3 K to the simulation data, we use the original algorithm (OA) and the NA to retrieve the emissivity from the simulation data. The RMSEs of the retrieved emissivity group ($\text{RMSE}_{\varepsilon,\text{gp}}$) are obtained by (18), as shown in Table I. At low temperature, the average RMSE of the emissivity retrieved by the OA is 0.0383, while the average RMSE of the emissivity retrieved by the NA is 0.00721. With the decrease in temperature, the RMSEs of the emissivity retrieved by the OA and the NA both increase; the NA's emissivity RMSE is mostly less than 0.01. The NA achieves significant advantages in the accuracy of low-temperature target emissivity inversion.

TABLE I

COMPARISON OF RETRIEVED EMISSIVITY RMSES BETWEEN THE NA AND THE OA FOR FIVE SAMPLES (SP1–SP5) AT FOUR LOW TEMPERATURES (240–270 K)

T (K)		SP1	SP2	SP3	SP4	SP5
270	OA	0.0234	0.0233	0.0236	0.0233	0.0231
	NA	0.0056	0.0067	0.0065	0.0057	0.0056
260	OA	0.0293	0.0292	0.0292	0.0294	0.0295
	NA	0.0065	0.0064	0.0067	0.0065	0.0065
250	OA	0.0399	0.0400	0.0401	0.0400	0.0401
	NA	0.0070	0.0071	0.0070	0.0069	0.0070
240	OA	0.0609	0.0610	0.0603	0.0608	0.0601
	NA	0.0094	0.0093	0.0092	0.0095	0.0092

TABLE II

COMPARISON OF RETRIEVED TEMPERATURE RMSES BETWEEN THE NA AND THE OA FOR FIVE SAMPLES (SP1–SP5) AT FOUR LOW TEMPERATURES (240–270 K)

T(K)		SP1	SP2	SP3	SP4	SP5
270	OA	0.1003	0.0903	0.0952	0.1004	0.1028
	NA	0.0908	0.0903	0.0923	0.0992	0.0901
260	OA	0.1022	0.1030	0.1243	0.1040	0.1064
	NA	0.0887	0.0868	0.0863	0.0901	0.0892
250	OA	0.1265	0.1713	0.1836	0.1390	0.1653
	NA	0.0823	0.0822	0.0816	0.0824	0.0826
240	OA	0.2245	0.2187	0.2397	0.1645	0.1904
	NA	0.2672	0.0880	0.0882	0.0902	0.0875

The RMSEs of the retrieved temperature group are calculated by (16) (Table II). The average temperature RMSE retrieved by the OA for low-temperature surfaces is 0.1426 K. The average temperature RMSE retrieved by the NA is 0.0968 K. With decreasing temperature, the RMSEs of the NA remain stable, while the RMSEs of the OA obviously increase. In general, the temperature inversion RMSEs of the NA is comparable to that of the OA, is around 0.1 K. The SP1 is an exception; the RMSEs of NA in temperature is even larger than that of OA at 240K, while the RMSEs of NA in emissivity is pretty less than that of OA at 240K. So the temperature inversion accuracy is not sensitive to the emissivity inversion accuracy for low-temperature surface.

D. Sensitivity to $\overline{NBCI}$ and $\overline{LACI}$

$\overline{\text{NBCI}}$ and $\overline{\text{LACI}}$ are defined as (10) and (12), respectively. They are two critical indices in the NA, reflecting the relations between the atmospheric downwelling radiance and ground leaving radiance. When the surface

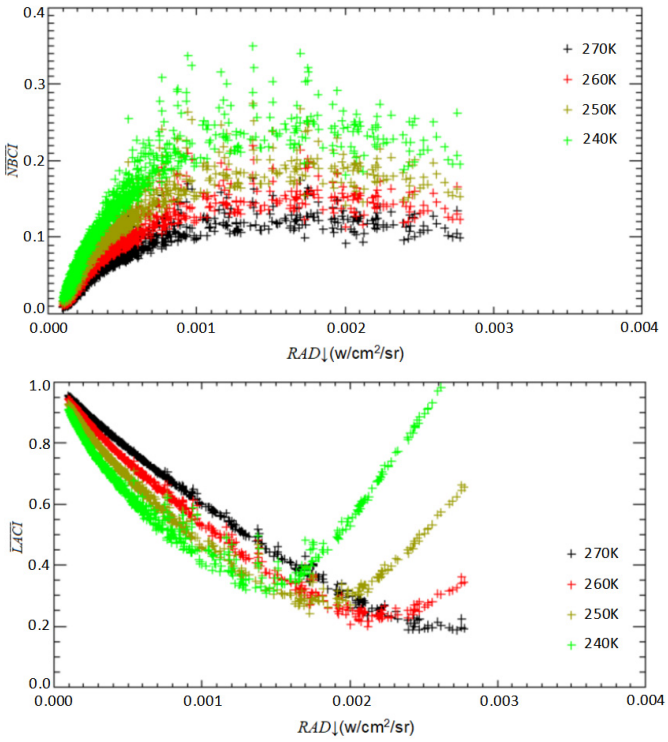

Fig. 3. Relationship between RAD↓ and $\overline{\text{NBCI}}$, $\overline{\text{LACI}}$.

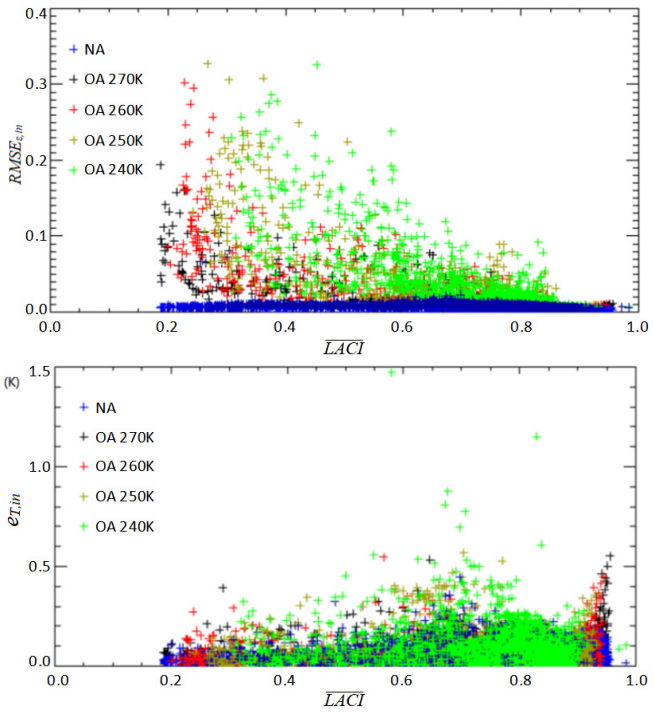

Fig. 4. Relation between $\overline{\text{LACI}}$ and $\text{RMSE}_{\varepsilon,in}$ as well as $e_{T,\text{in}}$.

temperature is given, the two indices have strong relations with the total downwelling radiance from the atmosphere. We calculate the radiance in the range of 800–1250 cm^{-1} by integrating the atmospheric down welling spectral radiation, denoted as RAD↓. Then, we can obtain the relationship between RAD↓ and $\overline{\text{NBCI}}$ as well as $\overline{\text{LACI}}$ (Fig. 3).

Different atmospheric profiles and different LSTs can lead to different simulation data. Each group of simulation data can obtain a value of $\overline{\text{NBCI}}$ as well as $\overline{\text{LACI}}$. We used black, red, yellow, and green dots to represent the results for the land surface with temperatures of 270, 260, 250, and 240 K, respectively.

It can be seen that $\overline{\text{NBCI}}$ increases and then decreases with RAD↓ (Fig. 3). Different surface temperatures also affect the $\overline{\text{NBCI}}$. Low surface temperatures cause high $\overline{\text{NBCI}}$. In contrast, $\overline{\text{LACI}}$ decreases first and then increases with RAD↓. The inflection point changes apparently with surface temperature, and the lower LST leads to the inflection point at the smaller value of RAD↓. The change of RAD↓ mainly comes from the radiance of atmospheric emissivity band. According to the definition of LACI [see (9) and (10)], when the radiance of the atmospheric emission band ($L_{\text{atm}\downarrow,\lambda}$) is close to the ground leaving radiation ($L_{\text{leiving},\lambda}$), the value of LACI is the lowest where the inflection point occurs. The ground leaving radiation is mainly determined by the surface temperature. Therefore, the position of the inflection point changes with the surface temperature.

The RMSEs of the retrieved individual emissivity spectrum ($\text{RMSE}_{\varepsilon,in}$) are calculated using (17). The absolute value errors of the retrieved temperature ($e_{T,\text{in}}$) are also calculated using (15).

The $\overline{\text{LACI}}$ and $\text{RMSE}_{\varepsilon,in}$ as well as $e_{T,\text{in}}$ are used to make the scatter plot (Fig. 4). The blue dots represent the results from the NA, while the black, red, yellow, and green dots represent the results from the OA for the surface temperatures of 270, 260, 250, and 240 K, respectively. It can be seen that the $\text{RMSE}_{\varepsilon,in}$ of NA is always low and not sensitive to $\overline{\text{LACI}}$, and they are mostly less than 0.01, while the $\text{RMSE}_{\varepsilon,in}$ of the OA is sensitive to $\overline{\text{LACI}}$. We find that the $\text{RMSE}_{\varepsilon,in}$ of the OA decreases with $\overline{\text{LACI}}$, and when $\overline{\text{LACI}}$ is greater than 0.8, the OA performs as well as the NA. For the retrieved temperature, $e_{T,\text{in}}$ is not sensitive to $\overline{\text{LACI}}$.

The $\overline{\text{NBCI}}$ and $\text{RMSE}_{\varepsilon,in}$ as well as $e_{T,\text{in}}$ are used to make scatter plots (Fig. 5). When $\overline{\text{NBCI}}$ is less than 0.04, $\text{RMSE}_{\varepsilon,in}$ decreases to 0.01. As both $\overline{\text{NBCI}}$ and $\overline{\text{LACI}}$ are related to downwelling radiance RAD↓, they are not independent. Fig. 3 shows that a low $\overline{\text{NBCI}}$ value corresponds to a low RAD↓ value, which corresponds to a high $\overline{\text{LACI}}$. The errors brought by $\overline{\text{LACI}}$ decrease when RAD↓ is low. Therefore, we focus on low $\overline{\text{LACI}}$ with a range from 0 to 0.04, where the $\overline{\text{LACI}}$ influence is small [Fig.5(c) and (d)]. Apparently, both the $e_{T,\text{in}}$ and the $\text{RMSE}_{\varepsilon,in}$ of the OA increase when $\overline{\text{NBCI}}$ decreases. They are higher than that of the NA when $\overline{\text{NBCI}}$ is less than 0.03.

E. Sensitivity to the Instrument Noises

We simulate instrumental random noise with the NETD in the range from 0 to 1.0 K at the interval of 0.1 K. The simulated noise is added to the simulated ground leaving radiance and downwelling radiance from the atmosphere. We retrieve emissivity using the NA and obtain the $\text{RMSE}_{\varepsilon,in}$ by (16). We calculate the average values of $\text{RMSE}_{\varepsilon,in}$ for

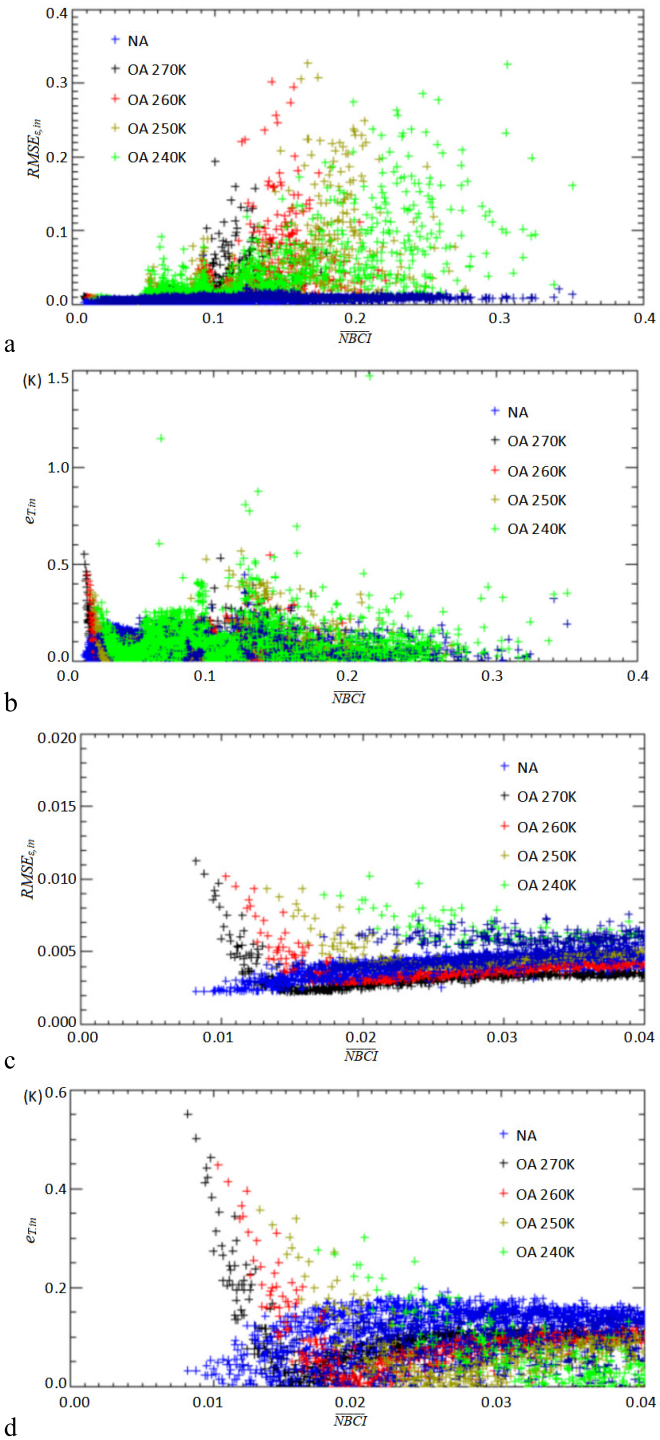

Fig. 5. Relation between $\overline{NBCI}$ and $RMSE_{\varepsilon,in}$ as well as $e_{T,in}$. (a) Scatter plot of $RMSE_{\varepsilon,in}$ against $\overline{NBCI}$. (b) Scatter plot of $e_{T,in}$ against $\overline{NBCI}$. (c) Detailed plot of $RMSE_{\varepsilon,in}$ against $\overline{NBCI}$ from 0.0 to 0.04. (d) Detailed plot of $e_{T,in}$ against $\overline{NBCI}$ from 0.0 to 0.04.

different LSTs of 270, 260, 250, and 240 K. We also calculate the stdev of each retrieval group. The average values and stdevs are plotted in Fig. 6. The NA is sensitive to instrument noise. The $\text{RMSE}_{\varepsilon,in}$ of the NA increases linearly with NETD. When the ground temperature is lower, the algorithm is more sensitive to instrument noise. When the NETD is less than 0.3, the $\text{RMSE}_{\varepsilon,in}$ of the NA remains less than 0.01 in emissivity.

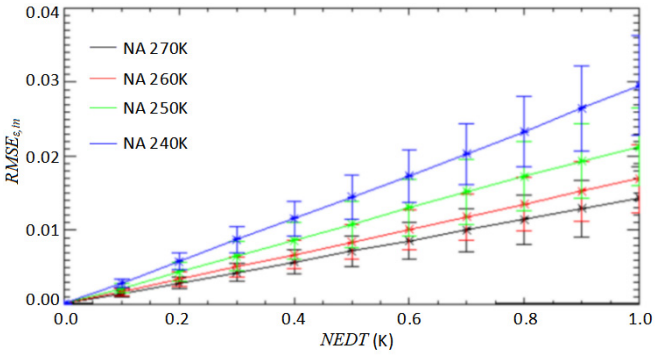

Fig. 6. NA sensitivity analysis to instrument noise.

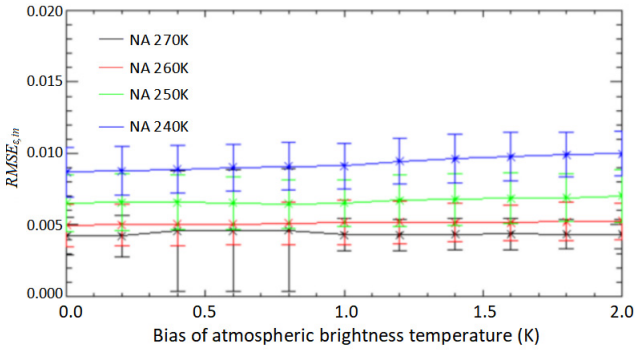

Fig. 7. NA sensitivity analysis to the uncertainties of downwelling radiance.

F. Sensitivity to the Uncertainties of Downwelling Radiance

We add the bias (noise) to downwelling radiance with brightness temperature changes from 0.0 to 2.0 K at the interval of 0.1 K. We retrieve emissivity using the NA and obtain the $\text{RMSE}_{\varepsilon,in}$ by (17). We calculated the average values of $\text{RMSE}_{\varepsilon,in}$ for different LSTs of 270, 260, 250, and 240 K, respectively. We also calculate the stdev of each retrieval group. The average values and stdevs are plotted in Fig. 7. Neither the average value nor the stdev of $\text{RMSE}_{\varepsilon,in}$ changes with the bias. The NA is not sensitive to the bias of downwelling radiance.

G. Sensitivity to the Uncertainties of Atmospheric Correction

To retrieve the LSE and LST from space-borne measurements, atmospheric correction is critical. The errors of atmospheric correction affect the downwelling/upwelling radiance of the atmosphere and atmospheric transmittance, eventually propagating to the retrieved emissivity.

To examine the algorithm's sensitivity to atmospheric correction, we added noise to the vapor profile from -10% to 10% with a step of 2%. The error of the retrieved emissivity increases linearly with the absolute error of the vapor profile [Fig. 8(a)]. We also added noise into the temperature profiles from -2.5 to 2.5 K with a step of 0.5. We can see that the error of the retrieved emissivity quickly increases with the absolute error of the temperature profile. The algorithm is more sensitive to atmospheric correction for low-temperature surfaces. To ensure emissivity inversion error less than 0.02,

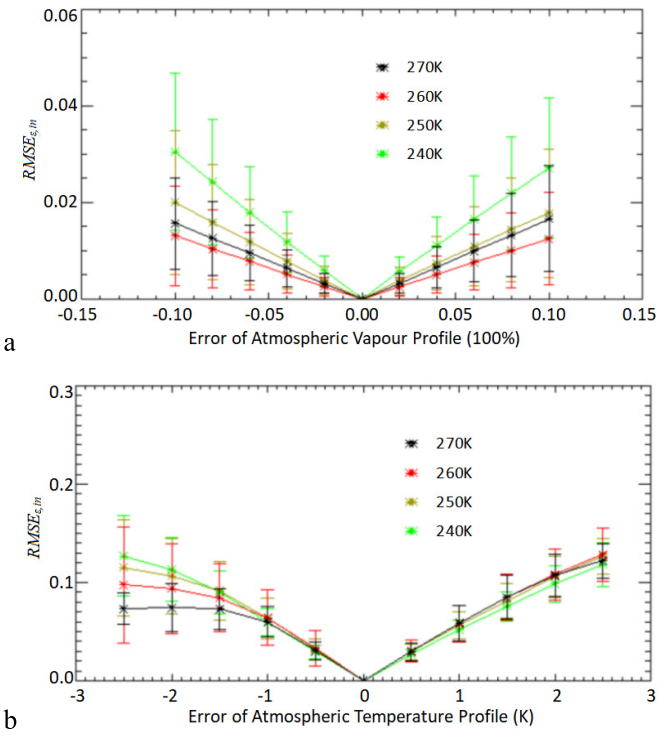

Fig. 8. NA sensitivity analysis to uncertainties of atmospheric correction. (a) Sensitivity analysis to uncertainties of atmospheric vapor profile. (b) Sensitivity analysis to uncertainties of atmospheric temperature profile.

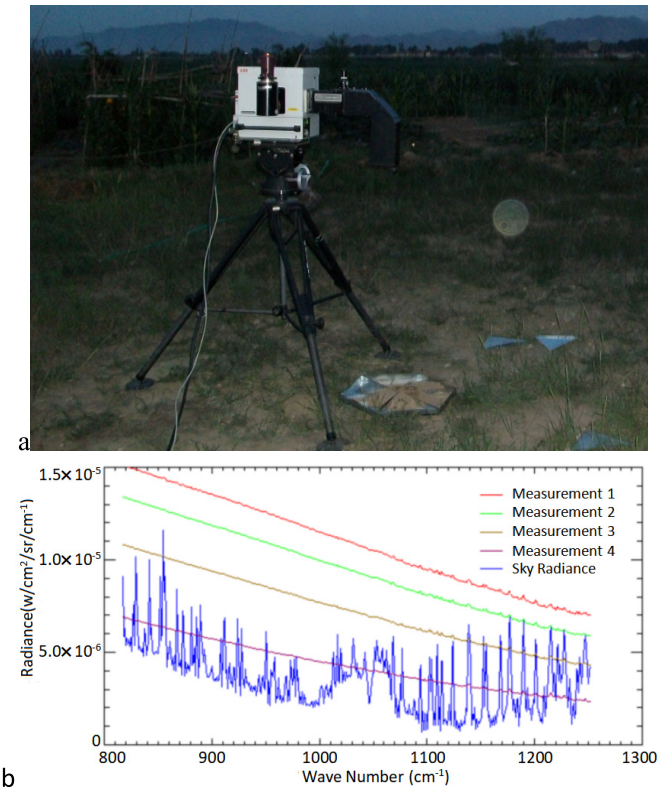

Fig. 9. (a) Experimental setup. (b) Radiance spectrum of four measurements.

we suggest that a good atmospheric correction with vapor error less than 6% and temperature error less than 0.5 K should be performed before this algorithm is used to retrieve emissivity for low-temperature areas from satellite-based measurements.

V. Field Experiment and Validation

The field experiment was conducted on August 10, 2009, at Huailai Remote Sensing Experimental Station of the Chinese Academy of Sciences (CAS) near Beijing, China, when the sky was clear and windless. We chose the soil surface as our research object. The soil type was brown loam. The low temperature of the soil was obtained by cooling it with different amounts of liquid nitrogen. An ABB BOMEN MR304 spectrometer was employed to measure the radiance. The spectrometer had a spectral range from 2 to 15 μm. Its noise equivalent spectral radiance (NESR) is better than $2.5 \times 10 - 9$ W/cm^2/sr/cm^{-1}. Its spectral resolution is adjustable from 1 to 32 cm^{-1}, it was set as 1 cm^{-1} in this experiment. A gold-coated diffuse reflective plate was used to collect the downwelling radiance from the sky. A blackbody M340 produced by Mikron cooperation was used for calibration. The emissivity of M340 is 0.99. The stability of its temperature is 0.1 °C [43]. We collected four groups of measured data. Each group included three types of data: 1) ground leaving radiance from the soil surface; 2) downwelling irradiance from the atmosphere; and 3) a pair of blackbody radiance with low and high temperatures for calibration.

The output of the spectrometer is digital number (DN), which needs to be calibrated by blackbody to convert DN value to radiance. The calibration formula is shown as (19), and the emissivity and temperature of the blackbody are known. Through Planck formula, the radiance of blackbody radiation can be calculated. The coefficients "a" and "b" in the calibration formula can be determined by two measurements of high and low temperature blackbody, respectively. Once these two coefficients have been determined, the DN values obtained from their measurements of leaving-ground radiance and downwelling atmospheric radiation can be substituted into the following formula to calculate the radiance of the measured target:

$$L_\lambda(\theta_r, \Phi_r) = a * \mathrm{DN} + b. \tag{19}$$

Four radiance spectra were measured [Fig. 9(b)]. The radiance of measurement 1 was obviously higher than the sky radiance. The radiance of measurement 4 was comparable to the sky radiance. We retrieved the emissivity and temperature using the OA and the NA separately. The surface temperatures of the four measurements varied from 311 to 259 K (Table III). The differences of temperatures retrieved by OA and NA are less than 1K. For the first three measurements when the surface temperature is greater than 280 K, the temperatures retrieved by OA and NA are nearly the same. When surface temperature is as low as 259 K, the retrieved temperature difference is around 0.53K, which creates the emissivity bias of 1% approximately [Fig. 10(d)].

An emissivity spectrum labeled as "Haplustall 85P4569" was selected from the JHU spectral library to exhibit as a reference in the retrieved emissivity figures (Fig. 10). The

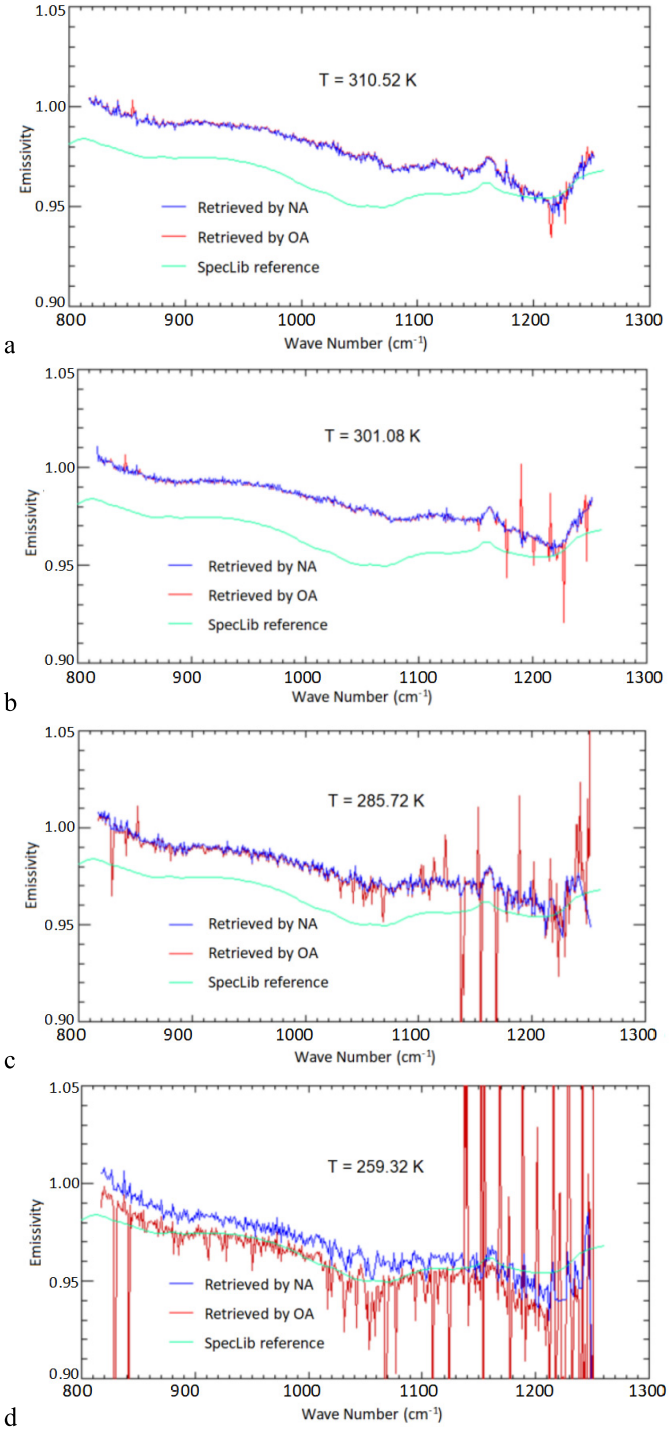

Fig. 10. Retrieved emissivity for the surface temperature of (a) 310.52K, (b) 301.08K, (c) 285.72K, and (d) 259.32K, separately.

emissivity retrieved from measurement 1 by the OA was very close to that retrieved by the NA [Fig. 10(a)]. As the surface temperature decreased, we could see that the number of singular values of emissivity spectra retrieved by the OA increased while the NA reduced the occurrence of singular values (Fig. 10). We took the emissivity retrieved from measurement 1 by the NA as the true value to evaluate the accuracy of the emissivity retrieved from other measurements by the OA

TABLE III
RETRIEVED TEMPERATURE BY THE OA AND NA

Measurement Number	1	2	3	4
Temperature retrieved by the OA (K)	310.50	301.09	285.75	258.79
Temperature retrieved by the NA (K)	310.52	301.08	285.72	259.32

TABLE IV
RMSE IN EMISSIVITY RETRIEVED BY OA AND NA

Measurement Number	1	2	3	4
RMSE of the OA	0. 00138	0. 00571	0. 01525	0. 29582
RMSE of the NA	0. 0	0. 00472	0. 00482	0. 05298

and NA. The RMSEs in the emissivity retrieved from each measurement are listed in Table IV. At normal temperature, the RMSE of the OA was similar to that of the NA for measurement 1 and measurement 2. At low temperatures, such as measurement 3 and measurement 4, the RMSE of the OA was large because of the singular values, while the RMSE of the NA was relatively small because it is free from singular values. Because there was frost covering the soil when the surface temperature was low, the true value of emissivity for low-temperature soil was no longer equal to that for normal temperature soil.

VI. CONCLUSION

When the ground leaving radiance of the low-temperature surface is comparable to the downwelling radiance from the sky, too many singular values degrade the accuracy of the retrieved emissivity [Fig. 10(d)]. To improve the accuracy of the retrieved emissivity for low-temperature areas, we formulate two indices: one characterizes the contrast between the surface radiance and sky downwelling radiance, and the other characterizes the contrast between the neighboring bands' radiance. These two indices are combined into a weight function to select the bands participating in the temperature/emissivity separation operation.

Numerical simulation experiments showed that for normal surface temperatures, the NA behaved as well as the OA, while for low surface temperatures, the NA effectively removed singular values in the retrieved emissivity and improved the accuracy. The RMSE in the emissivity retrieved by the NA was less than 0.01.

The NA is sensitive to the random noise of the instrument linearly. When the NETD of the instrument is less than 0.3 K, the RMSE of the emissivity is less than 0.01. The NA is not sensitive to the uncertainty of the downwelling radiance of the atmosphere when it is applied to ground-based measurements. The NA is very sensitive to the uncertainty

of atmospheric correction when it is applied to satellite-based measurements. To ensue emissivity inversion error less than 0.02, a very good atmospheric correction with vapor error less than 6% and temperature error less than 0.5 K needs performed. We recommend this NA to retrieve emissivity from ground-based measurements for low-temperature areas.

ACKNOWLEDGMENT

The authors are grateful to those who provided help in the field experiment: Yiqiao Zhi, Dr. Heshun Wang, and Dr. Hongzhang Ma. The authors thank three anonymous reviewers for their professional comments.

REFERENCES

[1] J. M. Norman and F. Becker, "Terminology in thermal infrared remote sensing of natural surfaces," *Agricult. Forest Meteorol.*, vol. 77, pp. 153–166, Dec. 1995.

[2] F. Becker and Z. Li, "Surface temperature and emissivity at various scales: Definition, measurement and related problems," *Remote Sens. Rev.*, vol. 12, nos. 3–4, pp. 225–253, Jan. 1995.

[3] X. Li, A. H. Strahler, and M. A. Friedl, "A conceptual model for effective directional emissivity from nonisothermal surfaces," *IEEE Trans. Geosci. Remote Sens.*, vol. 37, no. 5, pp. 2508–2517, Sep. 1999.

[4] Z.-L. Li *et al.*, "Satellite-derived land surface temperature: Current status and perspectives," *Remote Sens. Environ.*, vol. 131, pp. 14–37, Apr. 2013.

[5] J. Sun and L. Mahrt, "Determination of surface fluxes from the surface radiative temperature," *J. Atmos. Sci.*, vol. 52, no. 8, pp. 1096–1106, Apr. 1995.

[6] F. Jacob, A. Olioso, X. F. Gu, Z. Su, and B. Seguin, "Mapping surface fluxes using airborne visible, near infrared, thermal infrared remote sensing data and a spatialized surface energy balance model," *Agronomie*, vol. 22, no. 6, pp. 669–680, Sep. 2002.

[7] L. Zhou *et al.*, "A sensitivity study of climate and energy balance simulations with use of satellite-derived emissivity data over Nnorthern Africa and the Arabian Peninsula," *J. Geophys. Research: Atmos.*, vol. 108, no. D24, p. 4795, Dec. 2003, doi: 10.1029/2003JD004083.

[8] S. J. Hook, A. R. Gabell, A. A. Green, and P. S. Kealy, "A comparison of techniques for extracting emissivity information from thermal infrared data for geologic studies," *Remote Sens. Environ.*, vol. 42, no. 2, pp. 123–135, Nov. 1992.

[9] R. G. Vaughan, W. M. Calvin, and J. V. Taranik, "SEBASS hyperspectral thermal infrared data: Surface emissivity measurement and mineral mapping," *Remote Sens. Environ.*, vol. 85, no. 1, pp. 48–63, Apr. 2003.

[10] L. Kirkland *et al.*, "First use of an airborne thermal infrared hyperspectral scanner for compositional mapping," *Remote Sens. Environ.*, vol. 80, no. 3, pp. 447–459, Jun. 2002.

[11] B. Gao *et al.*, "Change in frozen soils and its effect on regional hydrology, upper Heihe basin, Northeastern Qinghai-Tibetan Plateau," *Cryosphere*, vol. 12, pp. 657–673, 2018.

[12] Z. Zhang, Q. Wu, X. Xun, B. Wang, and X. Wang, "Climate change and the distribution of frozen soil in 1980–2010 in Northern Northeast China," *Quaternary Int.*, vol. 467, pp. 230–241, Feb. 2018.

[13] D. A. Robinson, F. T. Keiinig, and K. F. Dewey, "Recent variations in Northern Hemisphere snow cover," *Proc. 15th Annu. Climate Diagnostics Workshop*, Asheville, NC, USA, 1991, pp. 219–224.

[14] T. Xuejin *et al.,* "Spatiotemporal changes in snow cover over China during 1960–2013," *Atmos. Res.*, vol. 218, pp. 183–194, Apr. 2019.

[15] R. D. Brown, "Northern hemisphere snow cover variability and change, 1915–97," *J. Climate*, vol. 13, pp. 2339–2355, Jul. 2000.

[16] C. C. Borel, "Surface emissivity and temperature retrieval for a hyperspectral sensor," in *Proc. IGARSS*, vol. 1, 1998, pp. 546–549.

[17] C. Borel, "Error analysis for a temperature and emissivity retrieval algorithm for hyperspectral imaging data," *Int. J. Remote Sens.*, vol. 29, nos. 17–18, pp. 5029–5045, Sep. 2008.

[18] Z.-L. Li *et al.*, "Land surface emissivity retrieval from satellite data," *Int. J. Remote Sens.*, vol. 34, nos. 9–10, pp. 3084–3127, 2013.

[19] Z.-L. Li, F. Becker, M. P. Stoll, and Z. Wan, "Evaluation of six methods for extracting relative emissivity spectra from thermal infrared images," *Remote Sens. Environ.*, vol. 69, no. 3, pp. 197–214, Sep. 1999.

[20] F. Becker and Z.-L. Li, "Temperature-independent spectral indices in thermal infrared bands," *Remote Sens. Environ.*, vol. 32, no. 1, pp. 17–33, Apr. 1990.

[21] K. Watson, "Spectral ratio method for measuring emissivity," *Remote Sens. Environ.*, vol. 42, no. 2, pp. 113–116, Nov. 1992.

[22] K. Watson, "Two-temperature method for measuring emissivity," *Remote Sens. Environ.*, vol. 42, no. 2, pp. 117–121, Nov. 1992.

[23] A. B. Kahle, D. P. Madura, and J. M. Soha, "Middle infrared multispectral aircraft scanner data: Analysis for geological applications," *Appl. Opt.*, vol. 19, no. 14, pp. 2279–2290, Jul. 1980.

[24] J. Cheng, S. Liang, Q. Liu, and X. Li, "Temperature and emissivity separation from ground-based MIR hyperspectral data," *IEEE Trans. Geosci. Remote Sens.*, vol. 49, no. 4, pp. 1473–1484, Apr. 2011.

[25] A. Gillespie, S. Rokugawa, T. Matsunaga, J. S. Cothern, S. Hook, and A. B. Kahle, "A temperature and emissivity separation algorithm for Advanced Spaceborne Thermal Emission and Reflection Radiometer (ASTER) images," *IEEE Trans. Geosci. Remote Sens.*, vol. 36, no. 4, pp. 1113–1126, Jul. 1998.

[26] A. Barducci and I. Pippi, "Temperature and emissivity retrieval from remotely sensed images using the grey body emissivity method," *IEEE Trans. Geosci. Remote Sens.*, vol. 34, no. 3, pp. 681–695, May 1996.

[27] P. S. Kealy and A. R. Gabell, "Estimation of emissivity and temperature using alpha coefficients," in *Proc. 2nd TIMS Workshop*, Pasadena, CA, USA, 1990, pp. 11–15.

[28] Z. Wan and Z.-L. Li, "A physics-based algorithm for retrieving land-surface emissivity and temperature from EOS/MODIS data," *IEEE Trans. Geosci. Remote Sens.*, vol. 35, no. 4, pp. 980–996, Jul. 1997.

[29] J. Cheng, S. Liang, J. Wang, and X. Li, "A stepwise refining algorithm of temperature and emissivity separation for hyperspectral thermal infrared data," *IEEE Trans. Geosci. Remote Sens.*, vol. 48, no. 3, pp. 1588–1597, Mar. 2010.

[30] N. Wang, H. Wu, F. Nerry, C. Li, and Z.-L. Li, "Temperature and emissivity retrievals from hyperspectral thermal infrared data using linear spectral emissivity constraint," *IEEE Trans. Geosci. Remote Sens.*, vol. 49, no. 4, pp. 1291–1303, Apr. 2011.

[31] J. Cheng, Q. Xiao, X. W. Li, Q. H. Liu, and Y. M. Du, "Multi-layer perceptron neural network based algorithm for simultaneous retrieving temperature and emissivity from hyperspectral FTIR data," *Spectrosc. Spectr. Anal.*, vol. 28, no. 4, pp. 780–783, Apr. 2008.

[32] K. Mao, J. Shi, H. Tang, Z.-L. Li, X. Wang, and K.-S. Chen, "A neural network technique for separating land surface emissivity and temperature from ASTER imagery," *IEEE Trans. Geosci. Remote Sens.*, vol. 46, no. 1, pp. 200–208, Jan. 2008.

[33] J. Cheng, Q. Liu, X. Li, Q. Xiao, Q. Liu, and Y. Du, "Correlation-based temperature and emissivity separation algorithm," *Sci. China Ser. D, Earth Sci.*, vol. 51, no. 3, pp. 357–369, Mar. 2008.

[34] P. M. Ingram and A. H. Muse, "Sensitivity of iterative spectrally smooth temperature/emissivity separation to algorithmic assumptions and measurement noise," *IEEE Trans. Geosci. Remote Sens.*, vol. 39, no. 10, pp. 2158–2167, Oct. 2001.

[35] *Description of the TIGR Dataset*. [Online]. Available: https://ara.lmd.polytechnique.fr/index.php?page=tigr

[36] A. M. Baldridge, S. J. Hook, C. I. Grove, and G. Rivera, "The ASTER spectral library version 2.0," *Remote Sens. Environ.*, vol. 113, no. 4, pp. 711–715, Apr. 2009.

[37] D. Manolakis *et al.*, "Longwave infrared hyperspectral imaging: Principles, progress, and challenges," *IEEE Geosci. Remote Sens. Mag.*, vol. 7, no. 2, pp. 72–100, Jun. 2019, doi: 10.1109/MGRS.2018.2889610.

[38] B. R. da Luz and J. K. Crowley, "Identification of plant species by using high spatial and spectral resolution thermal infrared (8.0–13.5 μm) imagery," *Remote Sens. Environ.*, vol. 114, pp. 404–413, Feb. 2010.

[39] S. Ullah, M. Schlerf, A. K. Skidmore, and C. Hecker, "Identifying plant species using mid-wave infrared (2.5–6 μm) and thermal infrared (8–14 μm) emissivity spectra," *Remote Sens. Environ.*, vol. 118, pp. 95–102, Mar. 2012.

[40] D. Harrison, B. Rivard, and A. Sánchez-Azofeifa, "Classification of tree species based on longwave hyperspectral data from leaves, a case study for a tropical dry forest," *Int. J. Appl. Earth Observ. Geoinformation*, vol. 66, pp. 93–105, Apr. 2018.

[41] B. M. Rankin, J. Meola, and M. T. Eismann, "Spectral radiance modeling and Bayesian model averaging for longwave infrared hyperspectral imagery and subpixel target identification," *IEEE Trans. Geosci. Remote Sens.*, vol. 55, no. 12, pp. 6726–6735, Dec. 2017.

[42] M. Black, T. R. Riley, G. Ferrier, A. H. Fleming, and P. T. Fretwell, "Automated lithological mapping using airborne hyperspectral thermal infrared data: A case study from anchorage island, antarctica," *Remote Sens. Environ.*, vol. 176, pp. 225–241, Apr. 2016.
[43] *Mikron M300 Series Blackbody Radiation Calibration*. [Online]. Available: https://www.docin.com/p-665351941.html
[44] J. M. Galve, C. Coll, V. Caselles, and E. Valor, "An atmospheric radiosounding database for generating land surface temperature algorithms," *IEEE Trans. Geosci. Remote Sens.*, vol. 46, no. 5, pp. 1547–1557, May 2008, doi: 10.1109/TGRS.2008.916084.

Yongming Du received the B.Sc. degree in geography from Yantai Normal College, Yantai, China, in 1999, the M.Sc. degree in cartography and remote sensing from Peking University, Beijing, China, in 2003, and the Ph.D. degree in cartography and remote sensing from the Institute of Remote Sensing Applications, Chinese Academy of Sciences (CAS), Beijing, in 2006.

He is an Associate Professor with the State Key Laboratory of Remote Sensing Science, Aerospace Information Research Institute (AIR), CAS. His research interest includes radiation transfer model in thermal infrared band.

Hua Li received the B.Sc. degree in geographic information system from the Xi'an University of Science and Technology, Xi'an, China, in 2004, the M.Sc. degree in cartography and geographic information system from Central South University, Changsha, China, in 2007, and the Ph.D. degree in cartography and geographic information system from the Institute of Remote Sensing Applications, Chinese Academy of Sciences (CAS), Beijing, China, in 2010.

He is an Associate Researcher with the State Key Laboratory of Remote Sensing Science, Aerospace Information Research Institute (AIR),CAS. His research interests focus on the retrieval and validation of land surface temperature (LST)/emissivity from satellite data.

Biao Cao received the B.Sc. degree in geographic information system from Beijing Forestry University, Beijing, China, in 2009, and the Ph.D. degree in cartography and geographic information system from the Institute of Remote Sensing and Digital Earth, Chinese Academy of Sciences (CAS), Beijing, in 2014.

He is a Research Assistant with the State Key Laboratory of Remote Sensing Science, Aerospace Information Research Institute (AIR), CAS. His research interests focus on the thermal radiation transfer model for complex land surface.

Zunjian Bian received the B.Sc. degree in geographic information system from the China University of Petroleum, Qingdao, China, in 2013, and the Ph.D. degree in cartography and remote sensing from the Institute of Remote Sensing and Digital Earth, Chinese Academy of Sciences (CAS), Beijing, China, in 2018.

He is a Post Doctor with the State Key Laboratory of Remote Sensing Science, Aerospace Information Research Institute (AIR), CAS. His research interests include the retrieval of component temperatures, and modeling and inversion of fine-scale land surface temperature (LST).

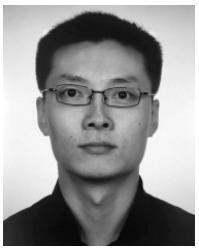

Jianming Zhao received the B.Sc. degree in photogrammetry and remote sensing major from the Changchun University of Aeronautics and Astronautics, Changchun, China.

He is a Research Assistant with the Beijing Institute of Remote Sensing Information, Beijing, China. His research interests focus on the retrieval and validation of land surface temperature (LST)/ emissivity from satellite data.

Qing Xiao received the B.Sc. degree from Jilin University, Changchun, China, in 1993, and the M.S. degree and the Ph.D. degree in remote sensing from the Institute of Remote Sensing Applications, Chinese Academy of Sciences (CAS), Beijing, China, in 1996 and 2002, respectively.

He is a Professor with the State Key Laboratory of Remote Sensing Science (SLRSS), Aerospace Information Research Institute (AIR), CAS. His research interests are quantitative processing and application of thermal infrared data and validation of remote sensing products.

Qinhuo Liu received the B.Sc. degree in hydrogeology and engineering geology from Southwest Jiaotong University, Chengdu, China, in 1988, and the M.Sc. degree in cartography and remote sensing and the Ph.D. degree in atmospheric physics from Peking University, Beijing, China, in 1994 and 1997, respectively.

He worked as a short-term Visiting Scholar with Institut National de la Recherche Agronomique (INRA), France, in 1998, Boston University, Boston, MA, USA, in 1999, the University of Maryland, College Park, MD, USA, in 2004, and George Mason University, Fairfax, VA, USA, in 2010. He was with the Institute of Remote Sensing and Digital Earth, Chinese Academy of Sciences (CAS), Beijing, from 1997 to 2016. He is a Professor and the Deputy Director of the State Key Laboratory of Remote Sensing Science, Aerospace Information Research Institute (AIR), CAS. His research interests focused on radiation transfer modeling for optical remote sensing and terrestrial parameter inversion from multisource remote sensing data.

Dr. Liu is a member of the American Geophysical Union (AGU) and the IEEE Geoscience and Remote Sensing Society (IEEE GRSS).

Yijian Zeng received the Ph.D. degree from the University of Twente, Enschede, The Netherlands, in 2012.

He is an Assistant Professor with Water Resources Department, Faculty of Geo-Information Science and Earth Observation (EO), University of Twente. His principal research interest is land–atmosphere interaction via understanding soil-water-plant-energy processes and how the interaction affects the climate system. His research focuses on developing the forward observation simulator, which integrates physically based process models and microwave emission and scattering models, and its application to assimilate EO data for sustainable water resources management within a data assimilation framework.

Zhongbo (Bob) Su received the M.Sc. degree in hydrological engineering from IHE, Delft, The Netherlands, and the Ph.D. degree in civil engineering from Ruhr University, Bochum, Germany, in 1989 and 1994, respectively.

He is a Professor of spatial hydrology and water resources management with the Faculty of Geo-Information Science and Earth Observation (EO), University of Twente, Enschede, The Netherlands. His research focuses on remote sensing and numerical modeling of land surface processes and interactions with the atmosphere, EO of water cycle and applications in climate, ecosystem, and water resources studies, and monitoring food security and water-related disasters.